ELSEVIER

Contents lists available at ScienceDirect

Reactive and Functional Polymers

journal homepage: www.elsevier.com/locate/react





Ultra-low wear in multifunctional Ti₃C₂T_x/PI composite films induced by tribo-chemistry mechanism

Guojing Chen^a, Shuai Jiang^a, Yufei Huang^a, Haosheng Pang^b, Xuan Yin^{c,*}, Chunpeng Chai^{a,*}

- a School of Materials Science and Engineering, Beijing Institute of Technology, Beijing 100081, China
- ^b Chinese Aeronautical Establishment, Beijing 100012, China
- ^c College of Mechanical and Electrical Engineering, Beijing University of Chemical Technology, Beijing 100029, China

ARTICLE INFO

Keywords: $Ti_3C_2T_x$ Polyimide Wear-resistant Lubrication Tribo-chemistry mechanism

ABSTRACT

 $Ti_3C_2T_x$ MXene was cooperated with polyimide (PI) to improve the wear resistance of the PI matrix under complex working conditions. Compared to the pristine PI, the $Ti_3C_2T_x/PI$ composites have excellent frictional properties, specifically, the coefficient of friction is 0.32 and the wear rate is 0.62×10^{-5} mm $^3/(N\cdot m)$. The composites formed a transfer film on the contact surface during the friction process, and the transfer film prevents direct contact between tribo-couples. The results studied by Raman and XPS showed that the transfer film contains TiO_2 that is derived from oxidized $Ti_3C_2T_x$. Moreover, the tribological mechanism has been summarized as two aspects: On one hand, the relative sliding of the $Ti_3C_2T_x$ lamellae transfers the sliding stress. On the other hand, a transfer film is created between $Ti_3C_2T_x/PI$ composites and steel ball during friction that prevents further wear of the material. All in all, two-dimensional MXene can effectively improve the wear resistance of the polymer matrix and has the potential to be used in friction-protective layers under complex working conditions.

1. Introduction

High-performance polymer protective layers (such as polyurethane, epoxy, and polyimide) play an important role in mechanical interfaces, cushioning substrates, and protective coatings [1]. Polyimide (PI) polymer material has light weight, wide temperature range, and has good self-lubrication performance widely involved in aerospace, land and sea transportation, petrochemical and microelectronics, etc. [2] Specifically, PI is usually used as a solid friction protection layer and a replacement for running parts in the traditional mechanical industry and high technology [3,4]. However, the single PI material has problems such as short wear life and low bearing capacity, which makes it difficult to attain the requirements of engineering applications for high wear resistance and long life of polymer materials [5,6].

One strategy to improve the properties of the PI matrix such as thermal conductivity, mechanical properties, and friction is to combine some reinforcing materials into the PI matrix [7,8]. Reinforcement materials are broadly categorized into three types based on their shape: zero-dimensional materials (SiO₂, TiO₂), one-dimensional materials (carbon nanotubes), and two-dimensional materials (fluorinated graphene, graphene, molybdenum disulfide). Among above mentioned many reinforcing materials, two-dimensional materials with high

specific surface area, excellent mechanical properties, and weak Van der Waals interaction between the nanosheets can effectively disperse the stress concentration under a heavy load [9,10]. During the rubbing process, the interlayer Van der Waals interaction of two-dimensional (2D) nanosheets is easily disrupted, leading to the peeling of their lamellas. The exfoliated lamellae reduce the shear resistance of the sliding interface and show its effect on self-lubrication. A stable and uniform transfer film is formed on the contact surface between tribo-couples, which separates the direct contact to improve the frictional performances of materials. Therefore, characters of transfer film and friction pairs are important factors to accelerate the friction reduction [11–14].

To investigate the influence of reinforcing materials on the tribological properties of the polymer matrix, researchers have conducted a series of works. Zhou et al. [15] prepared fluorinated graphene (FG)/PI composites by in situ polymerization and systematically investigated the effect of FG addition on the frictional properties of the PI matrix. Compared with that of the pure PI, the friction coefficient of the composites was reduced by 10.0% and the wear rate was reduced by more than 50.0% when the FG content was 0.5 wt%. During the friction process, not only amorphous carbon is formed, but also the F element on FG can form FeF₃ with Fe, both amorphous carbon and FeF₃ migrate to the transfer film together. Yang et al. [16] filled 20.0 wt% MoS₂ into

E-mail addresses: yinxuan@buct.edu.cn (X. Yin), chaicp@bit.edu.cn (C. Chai).

^{*} Corresponding authors.

thermosetting PI by hot-press sintering technique, resulting in a 47.6% reduction in friction coefficient and 75.6% reduction in wear of the composite. Hu et al. [17] used X-ray photoelectron spectroscopy to research the formation process of transfer film obtained from worn MoS₂/PI under high vacuum conditions. The results showed that the surface of the steel ball underwent severe wear and generated a large number of abrasive debris, while MoS₂ was oxidized to MoO₃. However, 2D materials such as graphene (GN) and MoS₂ are poorly dispersed in the PI matrix, making it difficult to build effective interfacial links with the matrix [18]. Therefore, the poorly dispersed GN and MoS2 are expected to be replaced by a better dispersed reinforcing material. MXene is a new 2D material similar in structure to graphene, with high specific surface area, abundant surface groups (-OH, -F, -O, etc.), and weak van der Waals interactions between nanolayers. MXene can avoid poor dispersion in composites, which usually occurs in PI composites modified by 2D materials with non-functional groups such as carbon, boron, and sulphur groups [19,20]. Therefore, the 2D lamellar material MXene has the potential to be used as a lubricant and wear-resistant reinforcing

In this work, $Ti_3C_2T_x$ MXene was innovatively used as a modifier to enhance the wear resistance of PI. HF was used as an etching agent for Ti_3AlC_2 , and the chemical composition and morphological structure of $Ti_3C_2T_x$ were characterized by SEM, TEM, XRD, and XPS. The effect of $Ti_3C_2T_x$ content on the friction and wear resistance of $Ti_3C_2T_x/PI$ composites was mainly investigated by friction tests. Additionally, we systematically obtain tribological mechanisms of $Ti_3C_2T_x/PI$ composites.

2. Experimental

2.1. Materials and chemicals

MAX phase (Ti₃AlC₂, Jilin 11 Technology Co.), HF (AR, Tianjin Oubokai Chemical Co.), Homophthalic dianhydride (PMDA, AR, Shanghai Sarn Chemical Technology Co.), 4,4'-Diaminodiphenyl ether (ODA, AR, Anhui Ze Sheng Technology Co.), *N*, *N*-Dimethylacetamide (DMAc, AR, Tianjin Guang Fu Technology Development Co.).

2.2. Preparation of $Ti_3C_2T_x$

In this work, $Ti_3C_2T_x$ was obtained by the method of HF etching [21]. Ti_3AlC_2 (1 g) was added to HF (20 mL, 40 wt%) in batches, the stirring speed and temperature were set to 500 rpm and 35 °C, respectively. After 24 h of reaction, the mixed solution was washed with deionized water and centrifuged at 3500 rpm for 5 min. The above washing operation was repeated until the pH of the supernatant liquid surface was neutral. Finally, the precipitate was freeze-dried at -69 °C for 8 h to obtain $Ti_3C_2T_x$.

2.3. Preparation of $Ti_3C_2T_y/PI$ composites

The Ti₃C₂T_x/PI composites were prepared in two steps:

(1) ODA was pre-dried under vacuum at 80 $^{\circ}$ C for 4 h. Similarly, PMDA was dried under vacuum at 100 $^{\circ}$ C for 4 h. ODA (4.005 g) was added to DMAc (50 mL) and sonicated for 30 min until completely dissolved. Equimolar ratios of PMDA (4.362 g) were added to the ODA solution in three batches with high-speed stirring, and the addition was completed within 30 min. After the last addition, the speed was reduced to 80 rpm and the reaction was carried out under an ice-water bath for 3 h to obtain the polyamidoacetic acid (PAA) solution with 12% solid content.

(2) ${\rm Ti_3C_2T_x}$ (0.40 wt%, 0.80 wt%, 1.20 wt%, 1.60 wt%, and 2.00 wt %) was ultrasonically dispersed in a certain amount of DMAc and then added to the above obtained PAA (8 g) with high-speed stirring for 30 min. The mixture was uniformly applied to 304 steel plates and dried in a vacuum drying oven for 4 h to evaporate the solvent. Finally, the above semi-cured film material was placed in a tube furnace for programmed

heating to fully thermalize (The heating procedure was 100 °C, 150 °C, 200 °C, 250 °C, 300 °C and 350 °C for 1 h, the heating rate was 2 °C/min). The detailed steps of $Ti_3C_2T_x/PI$ composites preparation are shown in Fig. 1. The $Ti_3C_2T_x/PI$ composites samples are named, the details are shown in Table S1.

2.4. Materials characterization

X-ray diffraction (XRD) patterns were recorded with a D8 Advance diffractometer. $\rm Ti_3C_2T_x$ nanosheets and transfer film were characterized with Thermo ESCALAB 250XI X-ray photoelectron spectroscopy (XPS) and LabRAM HR Evolution Raman Spectroscopy. Morphology and microstructures were observed with a scanning electron microscope (SEM) (Gemini 300) and JEM-2100plus high-resolution transmission electron microscope (HRTEM). Atomic force microscope (AFM) analysis of composite surface morphology using Bruker's Dimension XR model. FT-IR test was obtained from a NICOLET IS10 fourier transform infrared spectrometer (Nicolet, USA). Thermogravimetric analysis (TGA) of $\rm Ti_3C_2T_x/PI$ composites was collected by Shimadzu thermomechanical analysis system (The heating interval was 50–800 °C, the heating rate was 10 °C/min, N2 atmoball).

2.5. Friction measurements

The friction coefficient and wear rate of the samples were tested by the friction and wear tester model MS-M9000 (Lanzhou, China). Friction experiments were conducted at room temperature using a 4 mm diameter bearing steel (GCr15) ball as the upper counterpart ball, a cured PI composite as surface film, and a steel (304) disc as the underlying counterfacing plate. (The rotating speed is 300 r/min, and the rotating radius is 3 mm. The normal load is 5 N, and the experimental duration is 30 min).

3. Results and discussion

3.1. Preparation and structural characterization of Ti₃C₂T_x

 $Ti_3C_2T_x$ nanosheets were obtained by HF etching of $Ti_3AlC_2.$ As shown in Fig. 2a, the (104) strong diffraction peak corresponding to $2\theta\approx38.8^\circ$ is the peak of $Ti_3AlC_2.$ After HF etching, the (104) diffraction peak of Ti_3AlC_2 almost disappeared, while the (002) diffraction peak shifted from 9.69° to 9.37° [22]. The Bragg equation is as follows:

$$2dsin\theta = \lambda \tag{1}$$

where d is the crystal spacing and θ is the angle between incident light and the corresponding crystal plane. λ is the wavelength of the Xray. According to eq. 1, the layer spacing was expanded from 0.912 nm to 0.943 nm, which was the result of HF etching for the Al atomic phase in the structure of Ti₃AlC₂. After the etching procedure, some functional groups exist on the surface of Ti₃C₂T_x (Fig. 2b). The peaks located at 3430 cm⁻¹ and 1388 cm⁻¹ correspond to the stretching and bending vibrations of surface-OH, respectively. 1632 cm⁻¹ is the characteristic peak of C=O. The peaks located at 841 cm⁻¹ and 553 cm⁻¹ are the bending vibrations of the Ti-O-Ti bond and Ti-O bond, respectively. The above characteristic peak information indicates that the etching produces abundant functional groups on the Ti₃C₂T_x surface. The results are generally consistent with those previously reported in the literature [23]. The main characteristic Raman peak positions of Ti₃C₂T_x are between 100 cm⁻¹ and 800 cm⁻¹ (Fig. 2c). The A1g vibration mode of the MXene corresponds to 152 cm⁻¹ and 605 cm⁻¹, while the Eg vibration mode of the MXene corresponds to 214 cm⁻¹ and 402 cm⁻¹ respectively [24]. The characteristic peak of Al has not appeared in the Raman spectrum of $Ti_3C_2T_x$, indicating no residual Ti_3AlC_2 composition. In addition, two strong characteristic Raman peaks at 1360 cm⁻¹ and 1580 cm⁻¹ correspond to the *D*-band and G-band of the inorganic carbon material, respectively. The formation of the D-band is usually

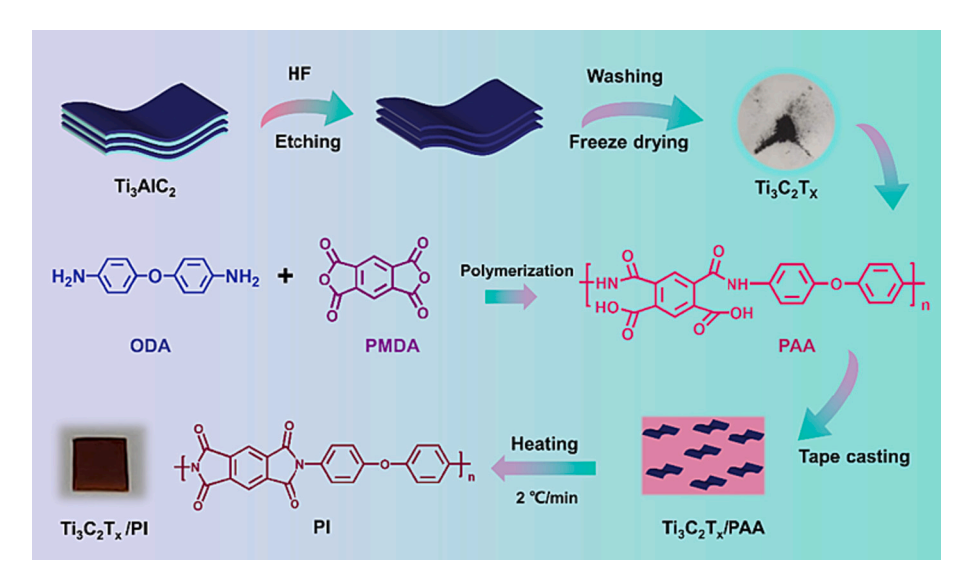


Fig. 1. Schematic diagram of the preparation of Ti₃C₂T_x/PI composites.

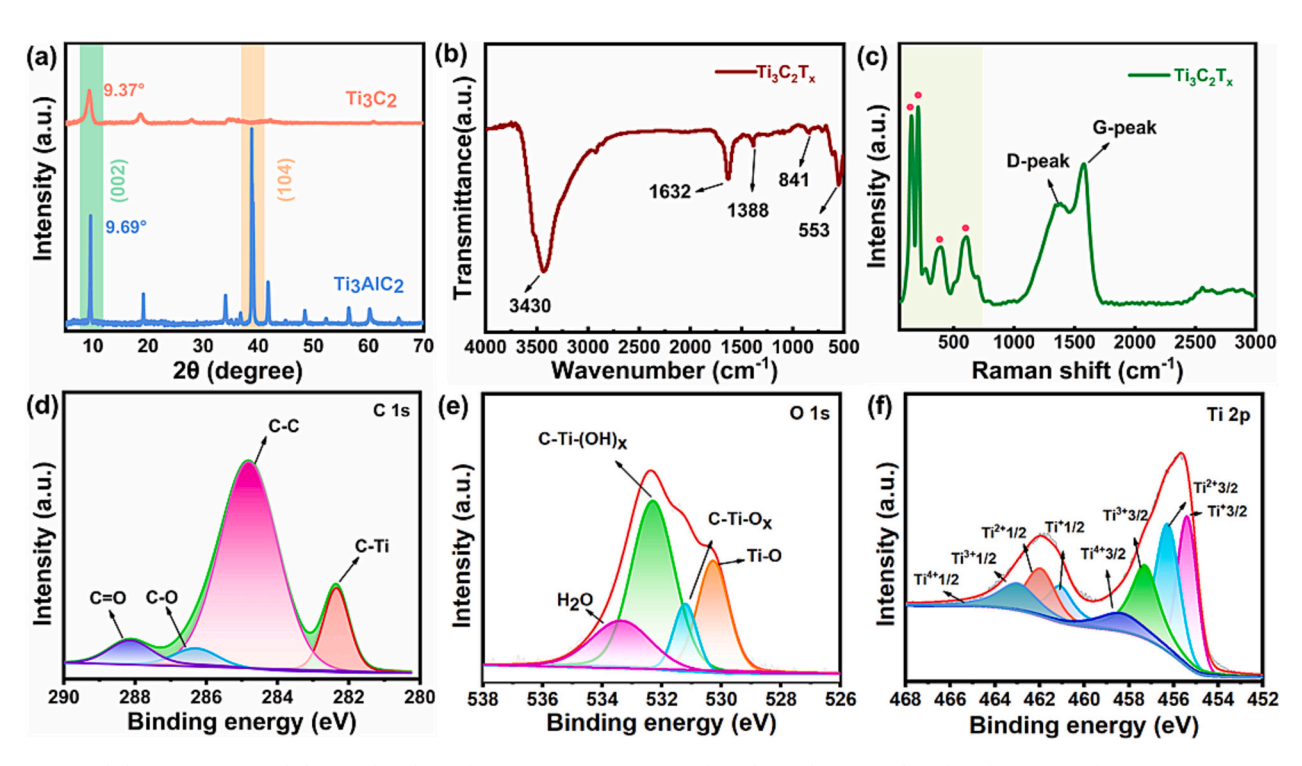


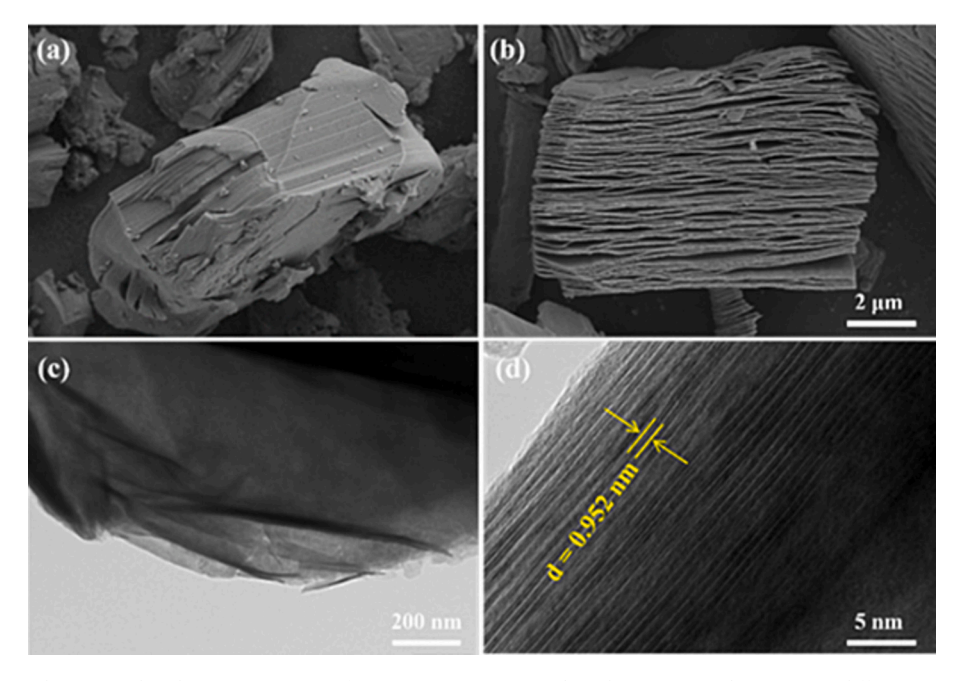
Fig. 2. Structural characterization and elemental analysis of MXene. (a) XRD patterns of Ti_3AlC_2 and $Ti_3C_2T_x$. (b) Infrared spectrum of $Ti_3C_2T_x$. (c) Raman spectrum of $Ti_3C_2T_x$. (d-f) C1s, O1s, and Ti2p XPS spectra of $Ti_3C_2T_x$, respectively.

considered to be caused by the sp^3 hybridization of graphene-like carbon atoms, and the G-peak is a characteristic peak caused by the vibration of the sp^2 -carbon phase in graphene-like. The ratio of D-peak to G-peak intensity indicates the amount of sp^3 hybridized atomic carbon in sp^2 -conjugated graphene-like materials. The ID/IG (degree of defects on the graphene-like surface [25]) intensity ratio of the $\mathrm{Ti}_3\mathrm{C}_2\mathrm{T}_x$ material prepared in this paper is 0.72, indicating a high degree of graphitization after etching. The appearance of the above Raman characteristic peaks suggests the successful preparation of $\mathrm{Ti}_3\mathrm{C}_2\mathrm{T}_x$.

The main constituent elements of $Ti_3C_2T_x$ are C, O, Ti, and F. (Fig. S1). The C1s narrow spectra were fitted to the split peaks, where 282.3 eV, 284.8 eV, 286.3 eV, and 288.1 eV represent the C—Ti, C—C, C—O, and C—O structures, respectively (Fig. 2d). In the O1s narrow spectrum, 530.3 eV, 531.2 eV, and 532.3 eV correspond to Ti—O, C-Ti-

Ox, and C-Ti-(OH)_x of the $Ti_3C_2T_x$ structure [26], respectively (Fig. 2e). The Ti2p orbitals form $2p_{1/2}$ and $2p_{3/2}$ orbitals due to energy level splitting (Fig. 2f), which are deconvoluted into the corresponding eight peaks in the narrow spectrum as Ti^+ (461.1 eV and 455.4 eV), Ti^{2+} (462.0 eV and 456.3 eV), Ti^{3+} (463.0 eV and 457.3 eV) and Ti^{4+} (464.0 eV and 458.3 eV) [27].

The microscopic morphology of $Ti_3C_2T_x$ was characterized by SEM and HRTEM. Ti_3AlC_2 shows a blocky structure under SEM, with tight arrangement between lamellae (Fig. 3a). $Ti_3C_2T_x$ is formed after HF etching, and the layer spacing is enlarged. Moreover, the structure of $Ti_3C_2T_x$ has a multilayer "accordion" shape (Fig. 3b). The TEM results in Fig. 3c and Fig. 3d also indicate that $Ti_3C_2T_x$ has a multilayer structure with stacking between layers, and the edges show a folded morphology. The lattice stripe spacing is about 0.952 nm, corresponding to the (002)



 $\textbf{Fig. 3.} \ \ \text{The (a,b) SEM and (c,d) HRTEM images of nanostructures. (a) } \ \ \text{Ti}_3\text{AlC}_2, \ \ \text{(b) } \ \ \text{Ti}_3\text{C}_2\text{T}_x \ \ \text{(c,d) } \ \ \text{Ti}_3\text{C}_2\text{T}_x \ \ \text{at different magnifications.}$

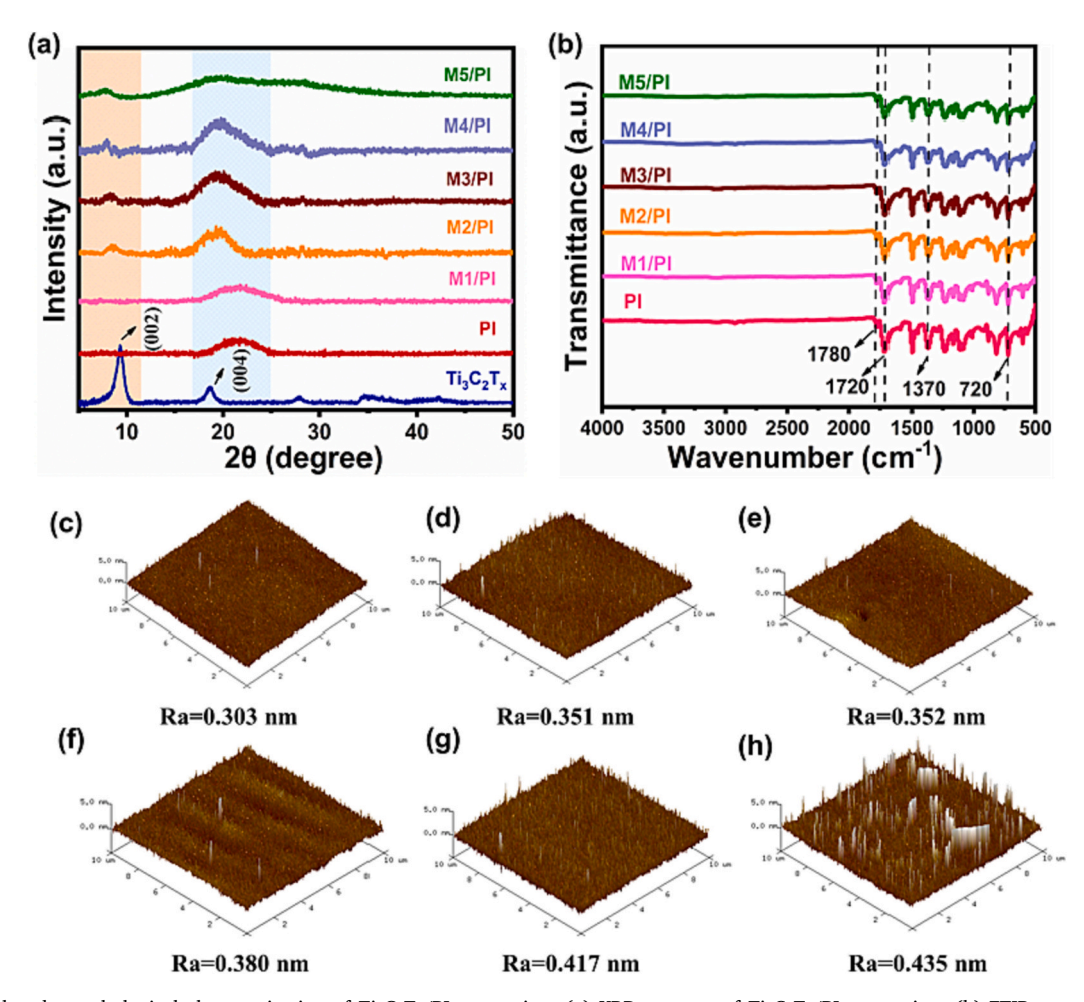


Fig. 4. Structural and morphological characterization of $Ti_3C_2T_x/PI$ composites. (a) XRD patterns of $Ti_3C_2T_x/PI$ composites. (b) FTIR spectrum of $Ti_3C_2T_x/PI$ composites. AFM images of (c)PI and (d-h) $Ti_3C_2T_x/PI$ composites.

crystal plane, which is consistent with the XRD characterization results.

3.2. Preparation and friction performance test of Ti₃C₂T_x/PI composites

The $Ti_3C_2T_x/PI$ composites were prepared by thermal imidization of the PAA and MXene blends. The crystal structure of the PI matrix and the phase composition of the $Ti_3C_2T_x/PI$ composites were characterized by XRD. PI and $Ti_3C_2T_x/PI$ composites show strong and broad characteristic peaks between $2\theta=17-25^\circ$, indicating the amorphous structure of PI.

After the addition of $Ti_3C_2T_x$, the diffraction peak of $Ti_3C_2T_x$ (002) was shifted from 9.37° to 7.74°, and the corresponding layer spacing was expanded from 0.943 nm to 1.141 nm. This change is due to the insertion of PI molecular chains into the $Ti_3C_2T_x$ lamellae, which disrupted the ordered stacking of $Ti_3C_2T_x$ [28,29]. In addition, the (004) diffraction peak of $Ti_3C_2T_x$ partially overlapped and broadened with the characteristic peak of PI (Fig. 4a).

The prepared PI and ${\rm Ti}_3{\rm C}_2{\rm T}_x/{\rm PI}$ composites were also characterized by FTIR spectroscopy. The wave numbers at 1780 cm $^{-1}$ and 1720 cm $^{-1}$ correspond to the asymmetric stretching and symmetric stretching vibrations of C=O in the acyl ring of the PI molecule. 1370 cm $^{-1}$ and 720 cm $^{-1}$ positions represent the stretching vibrations of C-N-C and the bending vibrations of C=O, respectively. However, the typical characteristic peaks of PAA were not seen at 3259 cm $^{-1}$ (stretching vibration of amide-NH-), 1655 cm $^{-1}$ (stretching vibration of amide C=O), and 1543 cm $^{-1}$ (overlapping peak of bending vibration of N—H with stretching vibration of C-NH), which indicates that PAA has been fully thermal imidized to PI (Fig. 4b) [30]. In other words, the above analysis proves the successful preparation of PI and ${\rm Ti}_3{\rm C}_2{\rm T}_x/{\rm PI}$ composites.

In the AFM images, the pure PI surface is smooth (surface roughness (Ra) = 0.303 nm). When the $T_{i3}C_2T_x$ content was lower than 1.20 wt%, the surface of the composites slightly changed. After the $T_{i3}C_2T_x$ content exceeded 1.20 wt%, pits and burrs appeared on the PI surface with increased surface roughness, which was caused by the agglomeration of $T_{i3}C_2T_x$ and the blocked solvent evaporation of PI during the curing process (Fig. 4c-h). Moreover, the introduction of $T_{i3}C_2T_x$ gives the composites excellent thermal stability (Fig. S2a-b), the temperature for a 5% loss of PI weight is 568.9 °C, while M5/PI requires 572.8 °C.

Therefore, the prepared ${\rm Ti}_3{\rm C}_2{\rm T}_x/{\rm PI}$ composites have the potential to be used at high temperatures.

The coefficient of friction and wear rate are important indexes in considering the tribological properties of a material. A low wear rate is a significant factor in improving the service life of a material, and a small coefficient of friction provides superior lubricity for the material. The average coefficient of friction of PI is 0.38 and the average wear rate is $2.68\times10^{-5}~\text{mm}^3/(\text{N}\cdot\text{m})$. Due to its poor wear resistance, PI will undergo large wear under sliding load. The appropriate amount of $Ti_3C_2T_x$ effectively reduced the friction coefficient. When $Ti_3C_2T_x$ was added at 0.80 wt%, the composite had the lowest friction coefficient with an average friction coefficient of 0.32 and an average wear rate of 0.62 \times $10^{-5}~\text{mm}^3/(\text{N}\cdot\text{m})$, which were 15.4% and 77.0% lower than that of the PI matrix, respectively (Fig. 5a-c). This excellent anti-friction and wear are due to the smoothing of the PI layer on the composite surface.

Subsequently, the exfoliated 2D lamellar $Ti_3C_2T_x$ was exposed to the sliding interface and adsorbed to the friction substrate, impeding direct contact between tribo-couples. In addition, the M3/PI has a wear rate of $0.60\times10^{-5}~\text{mm}^3/(\text{N}\cdot\text{m})$ with the shallowest depth of wear track (Fig. 5d). The wear track of PI and $Ti_3C_2T_x/\text{PI}$ composites was observed using SEM. The wear track of PI is wider that shows deeper furrows and scratches (Fig. S3a). After adding a small amount of $Ti_3C_2T_x$, the width of the wear track of the $Ti_3C_2T_x/\text{PI}$ composites becomes narrower. When the $Ti_3C_2T_x$ content was 0.80 wt% (Fig. S3c), the width and depth of the wear track of the composite reached the minimum value only a few pits and scratches appeared. When the $Ti_3C_2T_x$ content exceeded 1.20 wt%, the surface roughness increased due to the agglomeration of $Ti_3C_2T_x$ in the PI matrix, which in turn increased the friction coefficient and wear rate (Fig. S3a-d).

3.3. Tribo-chemistry mechanism of Ti₃C₂T_x/PI composites

The composition and structure of the transfer film play an important role in the frictional properties of materials. Morphological characterization and elemental analysis of the ground spots on the surface of the steel balls were performed using SEM. A thick and discontinuous polymer existed on the steel ball that was ground against the PI matrix and

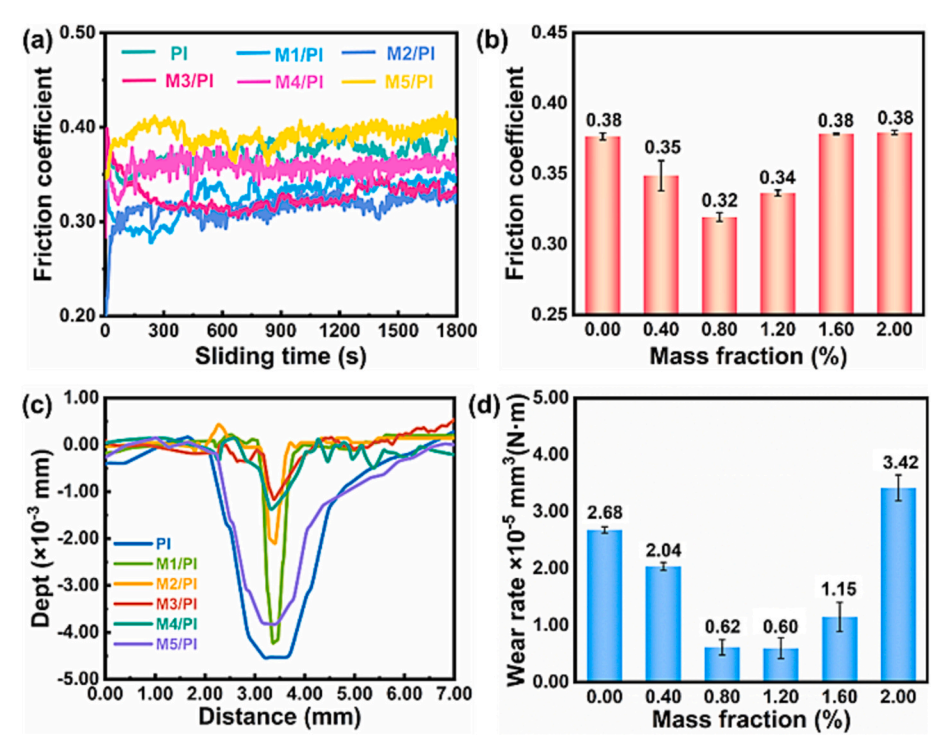


Fig. 5. Tribological performances of Ti₃C₂T_x/PI composites. (a) Friction curves. (b) Average friction coefficient. (c) Depth of the wear track. (d) Average wear rate.

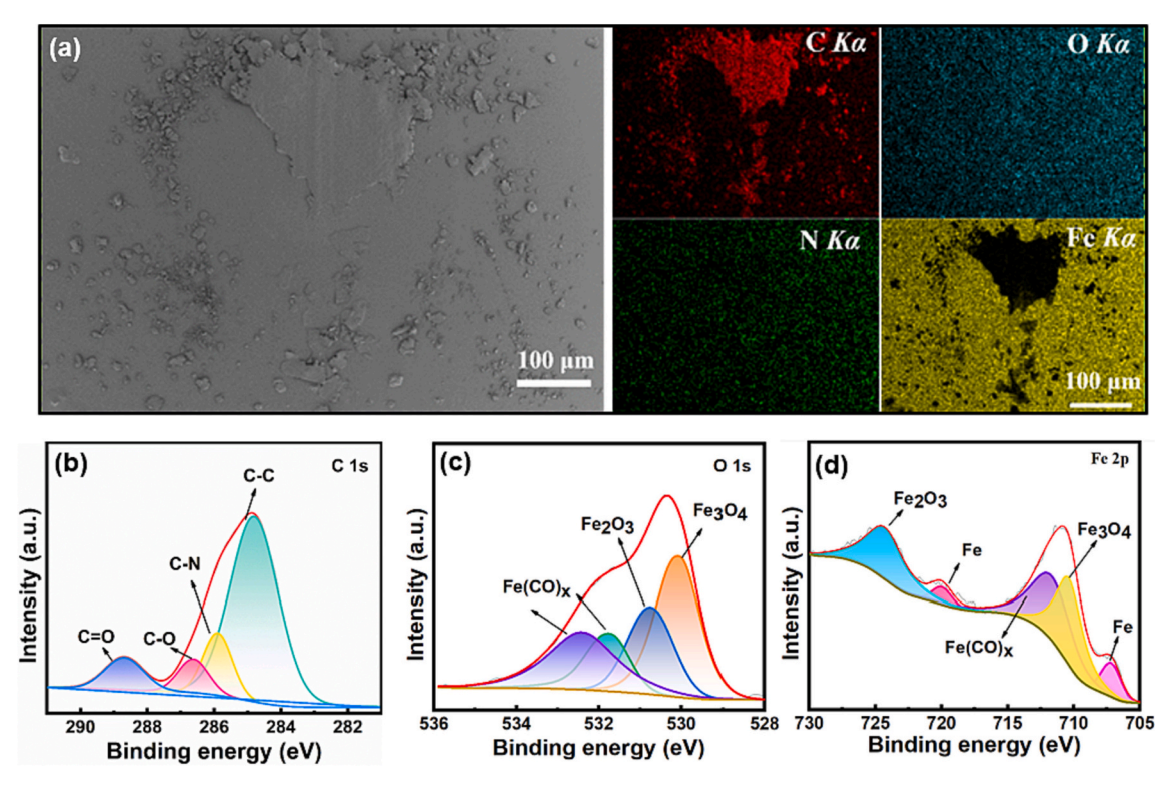


Fig. 6. Morphological characterization and elemental analysis of transfer film on the PI surface in $Ti_3C_2T_x/PI$ system. (a) SEM image of the PI grinding spot on the steel ball and corresponding elemental distribution. (b-d) C1s, O1s, and Si2p XPS spectra of transfer films, respectively.

compacted under shear stress (Fig. 6a). The EDS results show that the abrasive debris on the surface of the metal counterpart ball is mainly a polymer fragment, which softens and adheres to the metal counter face under the action of frictional heat.

We used XPS to further characterize the elemental composition and chemical structure of the transfer film. According to the XPS results, the constituent elements of the PI transfer film are mainly C, N, and O (Fig. S4). In the C1s narrow spectra, at 284.8 eV, 285.8 eV, 286.6 eV, and

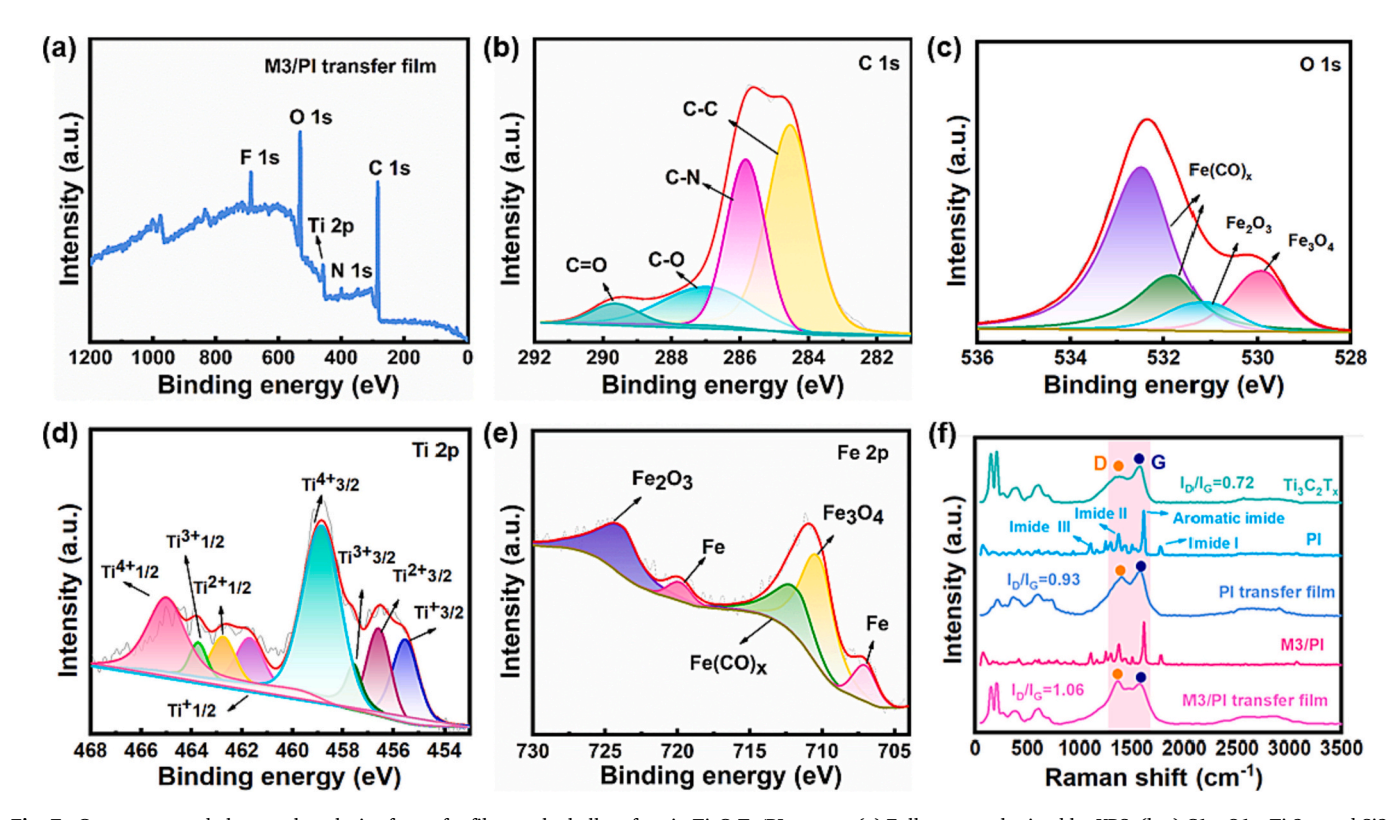


Fig. 7. Component and elemental analysis of transfer film on the ball surface in $Ti_3C_2T_x/PI$ system. (a) Full spectra obtained by XPS. (b-e) C1s, O1s, Ti 2p, and Si2p XPS spectra of transfer films, respectively. (f) Raman spectra of transfer films and $Ti_3C_2T_x/PI$ composites.

288.8 eV correspond to C—C, C—N, C—O, and C=O of the PI structure, respectively, which indicates that the PI abrasive chips are transferred to the metal pair during the friction process. The presence of C—C, C—N, C—O, and C=O in the C1s narrow spectra indicate the transfer of PI abrasive chips to the metal pair during the friction process (Fig. 6b).

The appearance of peaks of Fe_3O_4 and Fe_2O_3 in the narrow spectra of O1s and Fe2p proves that oxidation of the metal pair occurs during the friction process [31]. $Fe(CO)_x$ is also present in the narrow spectra of O1s and Fe2p, indicating that the formation of metal chelates between the PI matrix and the metal substrate during the friction process (Fig. 6c and d). The metal chelate allows for the transfer film's stable presence on the steel ball's surface [32,33].

The composite formed a transfer film on the steel balls after the friction test (Fig. S5). The EDS results showed that the transfer film contained elemental Ti, indicating that Ti₃C₂T_x can promote the formation of transfer film on the steel ball [34]. Fig. 7a-e illustrates the XPS spectra of transfer film. The presence of Ti and F elements was detected in the transfer films of the composites (Fig. 7a), indicating the transfer of Ti₃C₂T_x to the steel ball during the friction process. The XPS of the transfer film revealed that the Ti^{4+} $p_{3/2}$ and Ti^{4+} $p_{1/2}$ orbital peak intensities and peak areas in the Ti2p narrow spectra of the composites were significantly higher after the rubbing process, which was related to the oxidation of Ti₃C₂T_x (Fig. 7d) [35]. The narrow spectra of the mixed transfer film O1s showed significantly lower peak areas and peak intensities at 530.5 eV and 531.2 eV than the PI, respectively, which implies that the oxidation of steel ball was reduced after the addition of Ti₃C₂T_x. These results confirm that surface chemical reactions occurred at the contact surface during the friction process, and Ti₃C₂T_x underwent oxidation under high-speed sliding.

We further analysed the chemical structure of the transfer film by Raman spectroscopy (Fig. 7f). The transfer film of the pristine PI after the rubbing process contains D-band (1395 cm⁻¹) and G-band (1580 cm⁻¹). The D-band and G-band represent the amorphous carbon structure and the sp²-C phase in graphene, respectively. Meanwhile, the imide I-band (1778 cm⁻¹), imide II-band (1375 cm⁻¹), and imide III-band (1105 cm⁻¹) all showed different degrees of broadening and disappearance, implying that the molecular structure of the pristine PI was damaged and degraded during the friction process to produce amorphous carbon [36].

Due to the encapsulation of the PI matrix, the Raman characteristic peaks of $\rm Ti_3C_2T_x$ were not detected on the contact surface, and the positions of the outgoing peaks were the same as those of the PI. However, the Raman peak intensity of the composite transfer film is slightly different from that of PI. The Raman scattering peak of $\rm Ti_3C_2T_x$ appeared below 800 cm $^{-1}$ for the composite transfer film, indicating that $\rm Ti_3C_2T_x$ was transferred to friction pair along with PI The ID/IG increased from 0.93 (PI) to 1.06, confirming that the incorporation of $\rm Ti_3C_2T_x$ transformed the friction chemical product to an amorphous structure.

Based on the above analysis and characterization of $Ti_3C_2T_x/PI$ transfer film, the tribological mechanism of $Ti_3C_2T_x$ to improve the friction performances of PI substrate has been proposed in this paper (Fig. 8).

 $Ti_3C_2T_x$, a hard MXene material, effectively improves the thermal and frictional properties of the PI substrate. Due to the weaker van der Waals interaction between $Ti_3C_2T_x$ lamellae, the lamellae peel off under sliding stress. The peeling of the lamellae disperses and transfers the external stresses, further reducing the possibility of the material being damaged by heavy loads. The exfoliated $Ti_3C_2T_x$ transfer to the contact surface of the friction pair along with the abrasive chips of PI, forming a uniform transfer film. The transfer film can reduce the direct contact between tribo-couples, thus reducing the friction coefficient and wear rate of materials.

4. Conclusions

In summary, the multilayer Ti₃C₂T_x was obtained by etching with HF

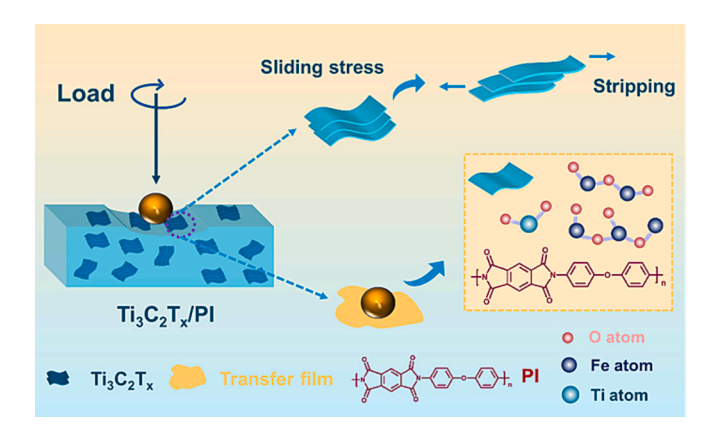


Fig. 8. The tribological mechanism of $Ti_3C_2T_x$ to improve the friction performance of PI.

and was innovatively added into the PAA precursor of PI to produce a series of Ti₃C₂T_x/PI composites by thermal imidization. The TGA and friction testing results prove that Ti₃C₂T_x can enhance the PI matrix's thermal stability and wear resistance. In particular, the wear rate of composites with Ti₃C₂T_x mass fraction of 1.20 wt% is reduced by 77.59% compared with PI. Furthermore, the appropriate amount of Ti₃C₂T_x can also reduce the friction coefficient in PI. When the Ti₃C₂T_x content is 0.80 wt%, the friction coefficient of $Ti_3C_2T_x/PI$ composites is reduced by 15.38% compared with PI. In addition, the tribological mechanism of Ti₃C₂T_x to improve the friction performance of PI is summarized as follows: Weaker van der Waals interactions between Ti₃C₂T_x flakes cause the flakes to peel under sliding stress, and the peeled flakes disperse and transfer the external stresses. Moreover, the transfer film formed on the counter faces can avoid direct contact between the friction pair. Therefore, the modification of PI by Ti₃C₂T_x is an effective strategy to enhance the frictional performance of the PI matrix, and the developed Ti₃C₂T_x/PI composites have great potential to be applied in the field of polymer protective layers or coatings under the condition of friction and wear.

CRediT authorship contribution statement

Guojing Chen: Writing – original draft. **Shuai Jiang:** Formal analysis. **Yufei Huang:** Data curation. **Haosheng Pang:** Investigation. **Xuan Yin:** Writing – review & editing. **Chunpeng Chai:** Project administration.

Declaration of Competing Interest

There are no conflicts to declare.

Data availability

The data that has been used is confidential.

Acknowledgements

This research was supported by the National Natural Science Foundation of China (51905295), the Liaoning Key Laboratory of Aeroengine Materials Tribology (LKLAMTF202304), and the Tribology Science Fund of State Key Laboratory of Tribology in Advanced Equipment (SKLTKF21B09).

Appendix A. Supplementary data

Supplementary data to this article can be found online at https://doi.org/10.1016/j.reactfunctpolym.2023.105744.

References

- [1] J.L. Wang, Q.Y. Huang, Y. Gao, N.N. Shi, Q.Q. Ge, H. Meng, M. Zhang, X.M. Wang, Chem. Mater. 34 (2022) 9119–9133.
- [2] D. Zhang, T.M. Wang, Q.H. Wang, C. Wang, J. Appl. Polym. Sci. 134 (2017) 45106.
- [3] D. Meis, S. Neumann, V. Filiz, Chem. Mater. 34 (2022) 3028–3041.
- [4] A. Roy, L.W. Mu, Y. Shi, Polym. Compos. 41 (2020) 2652–2661.
- [5] Z.X. Xu, X.D. Zhuang, C.Q. Yang, J. Cao, Z.Q. Yao, Y.P. Tang, J.Z. Jiang, D.Q. Wu, X.L. Feng, Adv. Mater. 28 (2016) 1981–1987.
- [6] F.X. Dong, G.L. Hou, F.X. Cao, F.Y. Yan, L. Liu, J.Z. Wang, Tribol. Int. 101 (2016) 291–300.
- Y.L. Zhao, X.W. Qi, Y. Dong, J. Ma, Q.L. Zhang, L.Z. Song, Y.L. Yang, Q.X. Yang, [7] Tribol. Int. 103 (2016) 599-608.
- [8] V.E. Ogbonna, P.I. Popoola, O.M. Popoola, S.O. Adeosun, J. Thermoplast. Compos. Mater. 36 (2023) 836-865.
- [9] G.X. Ding, H.X. Tai, C.X. Chen, C.F. Sun, Z.F. Tang, G.J. Cheng, X.L. Wan, Z. F. Wang, J. Appl. Polym. Sci. 139 (2021) 51947.
- [10] F.C. Jiang, T.M. Yu, C.H. Wang, M.X. Cao, Z.Q. Wang, Y.P. Chang, C.H. Guo, Polym. Adv. Technol. 32 (2021) 1363–1371.
- [11] C.H. Yang, Y.N. Wu, M. Nie, Q. Wang, Y.S. Liu, A.C.S. Appl, Mater. Interf. 13 (2021) 38656-38665.
- Γ12₁ Y.H. Wang, Z.M. Zhou, J.H. Zhang, J.Y. Tang, P.Y. Wu, K. Wang, Y.Z. Zhao, Coatings 10 (2020) 400.
- [13] C.H. Liu, X. Liao, W.L. Shao, F. Liu, B. Ding, G.H. Ren, Y.Y. Chu, J.X. He, Polymers 12 (2020) 836.
- [14] N. Farshchi, M. Gedan-smolka, Ind. Eng. Chem. Res. 59 (2020) 15121–15132.
 [15] S.G. Zhou, W.T. Li, W.J. Zhao, C. Liu, Z.W. Fang, X.L. Gao, Colloids Surf. A Physicochem. Eng. Aspects. 580 (2019), 123707.
- [16] M. Yang, C.H. Zhang, G.D. Su, Y.J. Dong, T.D. Mekuria, Q.T. Lv, Mater. Chem. Phys 241 (2020) 122034
- [17] H.J. Hu, Y. He, Q.H. Wang, L.M. Tao, Tribol. Int. 180 (2023), 108211.
- T. Huang, Y.S. Xin, T.S. Li, S. Nutt, C. Su, H.M. Chen, P. Liu, Z.L. Lai, A.C.S. Appl, [18] Mater, Interf. 5 (2013) 4878–4891.
- D. Johnson, Z. Qiao, E. Uwadiunor, A. Djire, Small. 18 (2021) 2106129.

- [20] P. Serles, M. Hamidinejad, P.G. Demingos, L. Ma, N. Barri, H. Taylor, C.V. Singh, C. B. Park, T. Filleter, Nano Lett. 22 (2022) 3356-3363.
- [21] P.G. Grützmacher, S. Suarez, A. Tolosa, C. Gachot, G.C. Song, B. Wang, V. Presser, F. Mücklich, B. Anasori, A. Rosenkranz, ACS Nano 15 (2021) 8216-8224.
- [22] W.X. Huang, Z.P. Li, D.D. Li, Z.H. Hu, C. Wu, K.L. Lv, Q. Li, Rare Metals 41 (2022) 3268-3300.
- N.U. Kiran, A.B. Deore, M.A. More, D.J. Late, C.S. Rout, P. Mane, B. Chakraborty, L. Besra, S. Chatterjee, A.C.S. Appl, Mater. Interf. 4 (2022) 2656–2666.
- [24] T. Hu, J.M. Wang, H. Zhang, Z.Q. Li, M.M. Hu, X.H. Wang, Chem. Chem. Phys. 17 (2015) 9997-10003.
- [25] R. Escribano, J.J. Sloan, N. Siddique, N. Sze, T. Dudev, Vib. Spectrosc. 26 (2001) 179_186
- [26] S.A. Haddadi, S.J. Hu, S. Ghaderi, A. Ghanbari, M. Ahmadipour, S.Y. Pung, S.B. Li, M. Feilizadeh, M. Arjmand, ACS Appl. Mater. Interfaces 13 (2021) 42074-42093.
- H. Riazi, M. Anayee, K. Hantanasirisakul, A.A. Shamsabadi, B. Anasori, Y. Gogotsi, M. Soroush, Adv. Mater. Interfaces 7 (2020) 1902008.
- [28] J. Liu, H.B. Zhang, X. Xie, R. Yang, Z.S. Liu, Y.F. Liu, Z.Z. Yu, Small. 14 (2018) 1802479.
- [29] N.N. Wang, H. Wang, Y.Y. Wang, Y.H. Wei, J.Y. Si, A.C.Y. Yuen, J.S. Xie, B. Yu, S. E. Zhu, H.D. Lu, W. Yang, Q.N. Chan, G.H. Yeoh, ACS Appl. Mater. Interfaces 11 (2019) 40512-40523.
- [30] Y. Zhou, S.Y. Zhang, F. Zheng, Q.H. Lu, Macromolecules 54 (2021) 9307-9318.
- [31] C. Hu, H.M. Qi, J.X. Yu, G. Zhang, Y.F. Zhang, H.T. He, J. Mater. Process. Technol. 281 (2020), 116602.
- [32] L. Zhou, H.M. Qi, Y. Lei, J.X. Yu, B.G. Guo, D. Zhang, Appl. Surf. Sci. 608 (2023), 155157.
- [33] Y.S. Lin, R. He, Y.K. Xu, J.J. Zhang, B. Wetzel, G. Zhang, Tribol. Int. 178 (2023), 108063.
- [34] Y.Z. Wang, T.C. Guo, E. Alhajji, Z.N. Tian, Z.X. Shi, Y.Z. Zhang, H.N. Alshareef, Adv. Energy Mater. 13 (2022) 2202860.
- M.L. Wang, S.X. Feng, C. Bai, K. Ji, J.X. Zhang, S.L. Wang, Y.Q. Lu, D.S. Kong, **[35]** Small. 19 (2023) 2300386.
- [36] P.K. Son, S.W. Choi, Mol. Cryst. Liq. Cryst. 546 (2011) 26-33.